



Full length article

ω phase acts as a switch between dislocation channeling and joint twinning- and transformation-induced plasticity in a metastable β titanium alloy

M.J. Lai ^{a,*}, T. Li ^b, D. Raabe ^a^a Max-Planck-Institut für Eisenforschung GmbH, Max-Planck-Str. 1, 40237 Düsseldorf, Germany^b Institute for Materials & ZGH, Ruhr-Universität Bochum, Universitätsstr. 150, 44801 Bochum, Germany

ARTICLE INFO

Article history:

Received 24 November 2017

Received in revised form

22 March 2018

Accepted 26 March 2018

Available online 31 March 2018

Keywords:

 β titanium

Deformation twinning

Martensitic transformation

Dislocation channeling

Transmission electron microscopy

ABSTRACT

We have investigated the twinning-induced plasticity (TWIP) and transformation-induced plasticity (TRIP) as well as the influence of ω phase on these two phenomena in a metastable β -type Ti–25Nb–0.7Ta–2Zr (at.%) alloy. We set off with two starting states: one is ω -free and the other one contains a high number density ($3.20 \pm 0.78 \times 10^{24} \text{ m}^{-3}$) of nanometer-sized ($\sim 1.23 \text{ nm}$) ω particles. Deformation experiments demonstrate that the plastic deformation of the ω -free alloy is mediated by stress-induced $\beta \rightarrow \alpha''$ martensitic transformation, {332} twinning and dislocation slip, where the former two induce joint TRIP and TWIP effects and the latter one carries the majority of the plastic strain. In the ω -enriched alloy, the ω particles fully suppress the TWIP and TRIP effects and promote localization of dislocation plasticity into specific ω -devoid channels. Atom probe tomography analysis reveals that the elemental partitioning between β and ω results in only subtle enrichment of solutes in the β matrix, which cannot sufficiently stabilize the matrix to prevent martensitic transformation and twinning. A new mechanism based on the shear modulus difference between β and ω is proposed to explain the suppression of TRIP and TWIP effects by ω particles.

© 2018 Acta Materialia Inc. Published by Elsevier Ltd. All rights reserved.

1. Introduction

Metastable β titanium alloys are of particular interest for structural applications in aerospace and biomedical industries [1]. After solution treatment in the β phase region and subsequent water quenching, the body-centered cubic (bcc) β matrix of these alloys exhibits low thermodynamic and elastic stability. This metastable state enables precipitation of secondary phases (α and/or ω) during aging, which lead to a significant increase in yield strength (above 1 GPa) [2,3]. In the past four decades, a large spectrum of α -hardened metastable β titanium alloys has been developed owing to the increasing demand for high-strength titanium alloys in the aerospace industry [4]. For these alloys, most of the studies were focused on the evolution of α precipitates during thermomechanical treatment, since the hardening effect of these precipitates depends on their morphology, size, distribution and volume fraction [1]. By properly tailoring the $\beta + \alpha$ microstructures,

the yield strength of the α -hardened alloys can be enhanced to a very high value (e.g., 1655 MPa) [3]. However, these alloys normally exhibit low work hardening and suffer from relatively low ductility (elongation to fracture below 10%), limiting their application [3,5].

In 2003, Saito et al. [6] claimed that a dislocation-free plastic deformation mechanism can be activated by tailoring the β matrix composition to attain extremely low β phase stability. Although their claim was extensively challenged by subsequent studies [7–11], this pioneering work triggered considerable attention to the dependence of the deformation mechanism on the β phase stability. Multiple deformation mechanisms, including {211} twinning [8,9,12,13], {332} twinning [12,14–16], stress-induced phase transformations ($\beta \rightarrow \alpha''$ and $\beta \rightarrow \omega$) [12–15] as well as dislocation slip [10–12] have been found in alloys with low β phase stability. It was also revealed that the {332} twinning and stress-induced $\beta \rightarrow \alpha''$ martensitic transformation can massively occur during plastic deformation, similar to {111} twinning and stress-induced $\gamma \rightarrow \epsilon$ martensitic transformation in high-Mn steels [17,18]. Such similarity implies that the twinning-induced plasticity (TWIP) and transformation-induced plasticity (TRIP) effects commonly seen in high-Mn steels [17,18] could potentially occur in metastable β

* Corresponding author.

E-mail address: m.lai@mpie.de (M.J. Lai).

titanium alloys as well. Recently, the TWIP and/or TRIP effects have actually been observed in Ti–12Mo [14,15], Ti–15Mo [19] and Ti–9Mo–6W [20] alloys, where these effects lead to very pronounced work hardening behavior and large ductility with uniform elongation above 20%. In TWIP/TRIP high-Mn steels, it had been demonstrated that the evolution of dislocation, twin and martensite substructures with increasing strain plays an important role in the work hardening behavior and hence the mechanical properties [17,18,21–23]. The evolution of these substructures as well as their interactions with each other in metastable β titanium alloys remain to be established.

It should be noted that the yield strength of the Ti–Mo-based alloys with TWIP and/or TRIP effects is relatively low (<600 MPa) [14,15,19,24], which also resembles the initial yield response of high-Mn steels [17,18]. To overcome the strength–ductility trade-off dilemma in metastable β titanium alloys, a possible route would be to introduce both the precipitation hardening effect and the TWIP and TRIP effects into the same alloy. This may be realized by precipitating secondary phases while maintaining a β matrix with low stability. In fact, concurrent α precipitate, {332} twinning and stress-induced $\beta \rightarrow \alpha''$ martensitic transformation have recently been reported in a β -type Ti–10 V–3Fe–3Al alloy, which sustained a metastable β matrix after holding it in the $\beta + \alpha$ phase region for a short time (5 min) [25,26]. Although the tensile properties of this alloy were not presented, these studies have paved a promising way for designing new metastable β titanium alloys with enhanced yield strength and improved ductility. It should also be noted that the precipitation of secondary phases (α and/or ω) may affect the TWIP and TRIP effects. This is another aspect that is not fully clarified yet.

In the present work, we study the deformation behavior of a metastable β -type Ti–25Nb–0.7Ta–2Zr (at.%) alloy (a derivative of gum metal [6]), with special focus on the evolution of {332} twin and α'' martensite at various strain levels as well as the influence of ω phase on the TWIP and TRIP effects. Our choice of this alloy was guided by two expectations: (i) it consists of a single β phase after water quenching from the β phase region, like the gum metal [6]; and (ii) its β phase stability is low enough to enable the activation of {332} twinning and stress-induced $\beta \rightarrow \alpha''$ martensitic transformation during straining. Here, two different starting states were designed by either water quenching or furnace cooling the solution-treated alloy, respectively. The mechanical response and the deformation microstructures of the alloy in these two states were examined by in situ and ex situ tensile deformation experiments. The influence of ω phase on the TWIP and TRIP effects as well as dislocation plasticity were discussed based on the elemental partitioning and shear modulus difference between β and ω .

2. Experimental

An arc-melted ingot with a nominal composition of Ti–25Nb–0.7Ta–2Zr (at.%) was homogenized at 1200 °C for 4 h under vacuum and then cold rolled at room temperature from 10 to 2 mm thickness (corresponding to a reduction in thickness of 80%). Two groups of sheets were cut from the as-cold rolled billet by electrical discharge machining (EDM). All of these sheets were solution treated at 1000 °C for 1 h under vacuum and, subsequently, one group of sheets was water quenched (WQ) and the other one furnace cooled (FC) to room temperature. The fast cooling rate for the WQ state was expected to suppress the precipitation of ω phase, while the much slower cooling rate for the FC state was expected to allow enough time for ω precipitation [27].

Flat dog-bone-shaped tensile specimens with a thickness of 1–2 mm and a gauge section of $4 \times 2 \text{ mm}^2$ were cut from the solution-treated sheets by EDM. The tensile axis was parallel to the

rolling direction (RD). Prior to tensile testing, one $4 \times 2 \text{ mm}^2$ surface of the tensile specimens was decorated with a graphite speckle pattern (spatial resolution: $\sim 30 \mu\text{m}$) for local strain field measurements. Tensile tests were carried out at an initial strain rate of $\leq 2.5 \times 10^{-3} \text{ s}^{-1}$ in a Kammrath and Weiss tensile stage and during the tests images of the graphite speckle pattern were acquired using two cameras at a speed of 1 frame/s. These images were correlated to calculate the local strain field using a digital image correlation technique [28] implemented in the ARAMIS software (Version v6.3.0–6). For examining the evolution of microstructures during deformation, in situ tensile tests were performed at an initial strain rate of $5 \times 10^{-4} \text{ s}^{-1}$ in a scanning electron microscope (SEM), where smaller tensile specimens with a gauge section dimension of $4 \times 1 \times 0.5 \text{ mm}^3$ were used. One $4 \times 1 \text{ mm}^2$ surface of these specimens was pre-polished for microstructure observation. The in situ tensile tests were interrupted at various strain levels for acquiring high-resolution backscattered electron (BSE) images.

Specimens for SEM imaging and electron backscatter diffraction (EBSD) mapping were ground using SiC paper with 600–4000 grit followed by precision polishing using a 50–100 nm colloidal silica suspension neutralized by H_2O_2 . Site-specific transmission electron microscopy (TEM) lamellae and needle-shaped atom probe tomography (APT) specimens were prepared using dual-beam focused ion beam (FIB) workstations (FEI Helios Nanolab 600 and FEI Helios G4 CX, respectively). The SEM imaging and EBSD mapping were carried out in a ZEISS CrossBeam 1540 XB field emission SEM operated at 15 kV. The TEM observation was conducted in a Philips CM 20 microscope and a JEOL JEM-2200FS field emission electron microscope operated at 200 kV. The latter microscope is equipped with an in-column Ω -type energy filter, which enables mapping of specimen thickness based on the electron energy loss spectroscopy (EELS) log-ratio technique [29,30]. The width of the energy-selecting slit used for mapping specimen thickness was 10 eV. The APT experiments were performed using a CAMECA LEAP

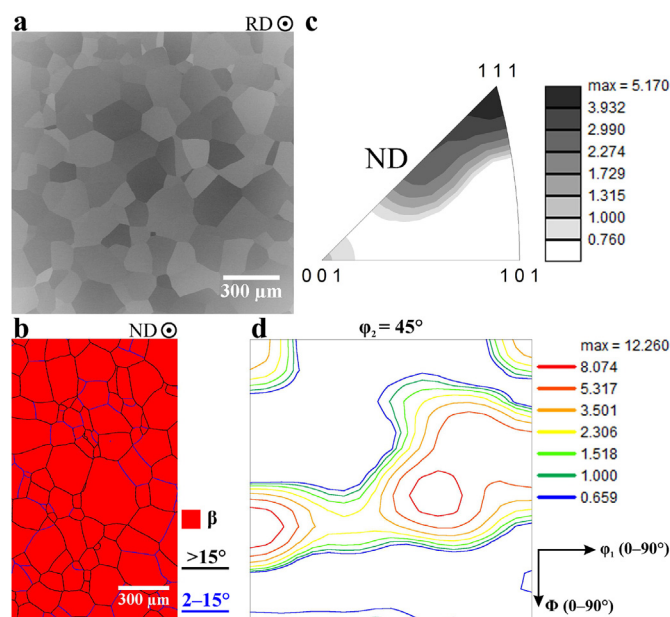


Fig. 1. Microstructure and crystallographic texture of the Ti–25Nb–0.7Ta–2Zr alloy subjected to furnace cooling after preceding cold rolling and solution treatment. (a) BSE image perpendicular to the rolling direction. (b) EBSD phase map perpendicular to the normal direction. The black and blue lines indicate the high- and low-angle grain boundaries, respectively. (c) Inverse pole figure along the normal direction. (d) Orientation distribution function map at $\phi_2 = 45^\circ$. (For interpretation of the references to color in this figure legend, the reader is referred to the Web version of this article.)

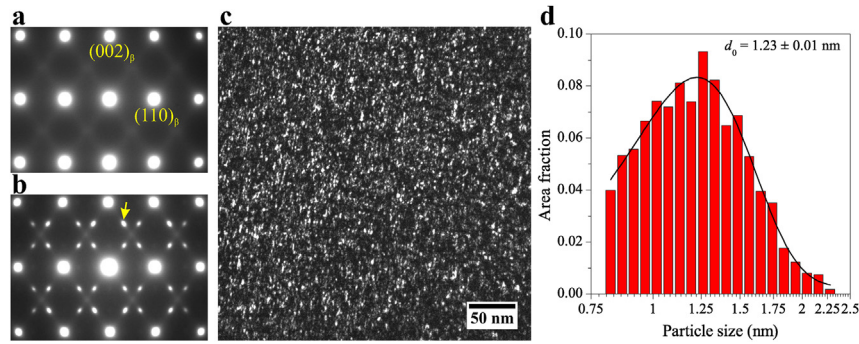


Fig. 2. TEM micrographs of the Ti–25Nb–0.7Ta–2Zr alloy subjected to water quenching (a) or furnace cooling (b–d), respectively, after preceding cold rolling and solution treatment. (a, b) Selected area electron diffraction patterns taken along the $[1\bar{1}0]_{\beta}$ zone axis. (c) Dark field image acquired using the ω reflection marked by an arrow in (b). (d) Size distribution of the ω particles shown in (c). d_0 represents the mean particle size.

5000XR instrument in voltage pulsing mode at a specimen temperature of 50 K with a pulse rate of 200 kHz, a target evaporation rate of 5 ions per 1000 pulses and a pulse fraction of 20%. The detection efficiency of this state-of-the-art instrument is ~52%. The APT data were reconstructed and analyzed using the IVAS (3.6.14) software.

3. Results

3.1. Initial microstructures

We found that the furnace cooled and water quenched states of the Ti–25Nb–0.7Ta–2Zr alloy exhibit almost identical grain size and texture. Hereafter, the alloy in these two states will be referred to as FC material and WQ material, respectively. Fig. 1 shows the initial microstructure and texture of the FC material. The BSE image of Fig. 1a, taken perpendicular to the RD, reveals equiaxed grain structures, where the grain size is about 125 μm as determined by a linear intercept method. EBSD scanning on the surface perpendicular to the normal direction (ND) reveals fully recrystallized β grains (Fig. 1b), while no secondary phases or annealing twins were observed. The inverse pole figure generated from the EBSD data, Fig. 1c, shows that the texture developed after cold rolling and solution treatment is characterized by a strong component with $\{111\}_{\beta}$ /ND. The orientation distribution function (ODF) map at $\varphi_2 = 45^\circ$, Fig. 1d, reveals that the texture consists of a dominant γ -fiber, i.e., $\{111\}_{\beta}$ /ND fiber, consistent with the typical recrystallization textures of bcc metals and alloys [31–33].

Fig. 2a shows the selected area electron diffraction (SAED) pattern of the WQ material, which was taken along the $[1\bar{1}0]_{\beta}$ zone axis. In addition to the distinct reflections from the bcc β matrix, very faint reciprocal lattice streaks along $\langle 112 \rangle_{\beta}$ directions as well as diffuse scattering at $1/2 \{112\}_{\beta}$ positions are visible in this pattern. However, reflections from ω phase, i.e., local intensity maxima at $1/3$ and $2/3 \{112\}_{\beta}$ positions, are not observed (a detailed intensity profile along the $[1\bar{1}2]_{\beta}$ direction is presented in Supplementary Fig. S1). During the corresponding TEM dark field imaging, we did not find any ω phase even after a long exposure time (>30 s). This demonstrates that there is no ω phase in the WQ material. A recent theoretical study [34] has revealed that the softening of the N -point phonons (associated with displacements of neighboring $\{1\bar{1}0\}$ planes in opposite $\langle 110 \rangle$ directions) within a bcc crystal structure can lead to streaking and diffuse scattering similar to that observed in Fig. 2a. This indicates that the elastic stability of the present WQ β matrix is relatively low.

For the FC material, secondary ω phase precipitated during the slow cooling process. This is manifested by the $[1\bar{1}0]_{\beta}$ SAED pattern

of this material, Fig. 2b, where the pronounced diffraction intensity maxima at $1/3$ and $2/3 \{112\}_{\beta}$ positions give direct evidence of the existence of ω precipitates [27,35]. Since the precipitation was thermally activated, the four variants of the ω phase should have formed with equal population [36,37]. A TEM dark field image of one of the ω variants, acquired using the ω reflection marked by an arrow in Fig. 2b, is shown in Fig. 2c. The ω precipitates are visualized as nearly spherical particles and they are homogeneously distributed within the β matrix. Fig. 2d shows their size distribution, where 2249 ω particles were measured. The mean particle size d_0 is around 1.23 nm. The number density of the ω particles, n , was measured in 36 separate regions with an equal area of $27.19 \times 27.19 \text{ nm}^2$ and an average thickness of 98–118 nm by taking into account all four ω variants [30]. In each region, the inter-particle spacing l and the volume fraction f of the ω particles were calculated by $l = 1/\sqrt{2d_0n}$ [38] and $f = \pi nd_0^3/6$, respectively. The mean number density n_0 , inter-particle spacing l_0 and volume fraction f_0 were estimated to be $3.20 \pm 0.78 \times 10^{24} \text{ m}^{-3}$, $11.53 \pm 1.37 \text{ nm}$ and $0.31 \pm 0.08\%$, respectively.¹

3.2. Mechanical response

Fig. 3a shows the representative tensile engineering stress-strain (σ - ϵ) curves of the WQ and FC materials. The 0.2% offset yield strength (YS), ultimate tensile strength (UTS) and elongation to fracture (ETF) acquired from these curves are listed in Table 1. The YS of the ω -enriched FC material is 40% higher than that of the ω -free WQ material. This can be explained by the precipitation hardening effect of the ω particles in the former material. After yielding, the FC material behaves like the ω -enriched gum metal [27], exhibiting a long plateau in the σ - ϵ curve with rather low work hardening. In contrast, the WQ material shows very pronounced work hardening behavior after yielding. As a consequence, its UTS is 290 MPa higher than its YS. Similar to other as-quenched metastable β -type Ti–Nb-based alloys, the present WQ material also exhibits a secondary yielding phenomenon (at $\epsilon \sim 4.41\%$), indicating that stress-induced $\beta \rightarrow \alpha''$ martensitic transformation occurred during the tensile deformation [39–43].

Fig. 3b displays the work hardening rates versus true strain and the true stress-strain (σ_T - ϵ_T) curves of the WQ and FC materials. With increasing strain, three general work hardening stages, labelled as I–III in Fig. 3b, can be distinguished for both materials: Stage I and Stage III are characterized by a continuously decreasing work hardening rate, while Stage II exhibits nearly constant work

¹ The errors represent standard deviation of the mean.

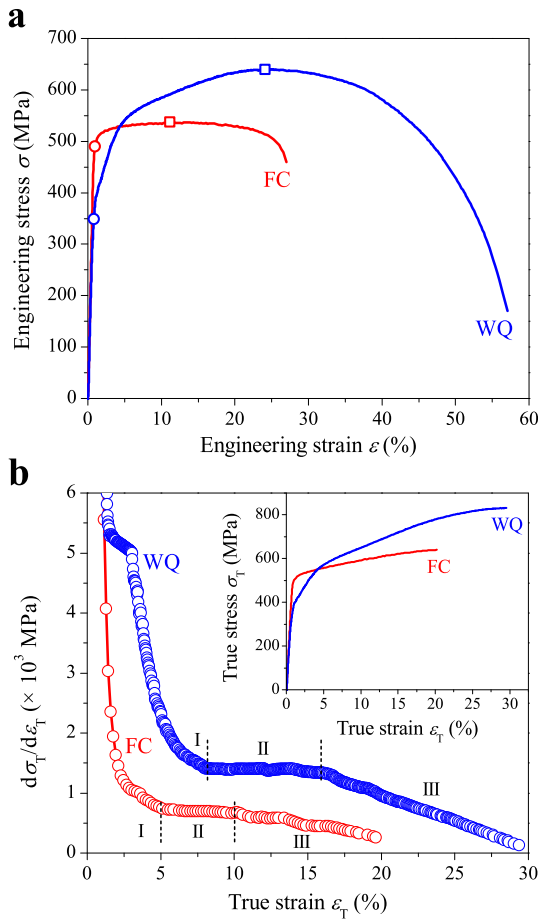


Fig. 3. Mechanical response of the Ti–25Nb–0.7Ta–2Zr alloy in water quenched (WQ) and furnace cooled (FC) states. (a) Tensile engineering stress–strain curves. The open circles and squares mark the 0.2% offset yield strength and the ultimate tensile strength, respectively. (b) Work hardening rates as a function of the true strain. The inset shows the true stress–strain curves.

Table 1

Mechanical properties of the Ti–25Nb–0.7Ta–2Zr alloy in water quenched (WQ) and furnace cooled (FC) states. YS, UTS, UE and ETF represent the 0.2% offset yield strength, ultimate tensile strength, uniform elongation and elongation to fracture, respectively.

State	YS	UTS	UE	ETF
WQ	350 MPa	640 MPa	25%	57%
FC	490 MPa	540 MPa	13%	27%

hardening behavior. Similar phenomena have commonly been observed in various steels [44] and also in β -type Ti–15 wt% Mo alloy [19]. The uniform elongation (UE), i.e., the elongation until the onset of necking, can be determined by $d\sigma_T/d\varepsilon_T = \sigma_T$ according to the Considère criterion [38]. Due to the significantly higher work hardening rate of the WQ material over the entire post-yielding strain range, its UE is almost twice that of the FC material (Table 1). Fig. 3b also shows that an additional inclined plateau ($\varepsilon_T = 1.6$ –3%) occurs within Stage I of the WQ material. Given that the work hardening behavior is controlled by the active deformation mechanisms [21,22,45], these differences in the work hardening behavior between the ω -free WQ and ω -enriched FC materials imply that the precipitation of ω phase has also led to changes in the deformation mechanisms. In the following section, we reveal the specific deformation mechanisms operating in these

two materials by examining their deformation microstructures.

3.3. Deformation microstructures

3.3.1. Deformation twin and stress-induced martensite in the WQ material

To unveil the origin of the very pronounced work hardening behavior of the ω -free WQ material, we examined the deformation microstructures of this material at different strain levels. As mentioned above, stress-induced martensitic transformation is supposed to occur in this material in the early stage of plastic deformation, resulting in a double-yielding phenomenon (Fig. 3a). The first yield point has commonly been reported to correspond to the critical stress for inducing $\beta \rightarrow \alpha''$ martensitic transformation [39–43]. Kim et al. [40] also claimed that the second yield point corresponds to the onset of dislocation slip. Here, we performed in situ SEM straining experiments to study the evolution of deformation microstructures between these two yield points, as shown in Fig. 4. When the true strain in the WQ material accumulates to 1.04% (slightly beyond the first yield point), Fig. 4a, two types of deformation bands occur, one with distinct topographic contrast ($\{332\}$ twin) and the other with only weak channeling contrast (α'' martensite) [46]. Unambiguous identification of these two types of deformation bands by TEM and EBSD is presented in Fig. 5 and Fig. 6, which will be described in detail later. The area fraction of the $\{332\}$ twins measured from Fig. 4a is around 0.56%. On continuously increasing the true strain to 2.91%, the evolution of deformation microstructures is characterized by the proliferation of both $\{332\}$ twin and stress-induced α'' martensite, as shown in Fig. 4b and c. Most of the twins nucleate from grain boundaries or pre-formed twin boundaries and propagate straightly to other grain boundaries or twin boundaries, leading to grain fragmentation. The area fraction of the $\{332\}$ twins increases almost linearly with the increase of the true strain, being around 4.51% in Fig. 4b and around 10.47% in Fig. 4c. The area fraction of the α'' martensite plates, however, cannot be quantitatively determined due to their too weak channeling contrast in most of the grains (caused by large deviations from the Bragg condition [46]). Upon completely unloading from the loading state of Fig. 4c, many α'' martensite plates reversely transform into the parent β phase and most of the $\{332\}$ twins are subjected to a slight reduction in thickness (partial detwinning), as illustrated in Fig. 4d. The area fraction of the $\{332\}$ twins is thus reduced to around 8.07%. The deformation microstructures remained after unloading, including α'' martensite plates and $\{332\}$ twins, result in a residual true strain of 1.25% (Fig. 4d). Similar incomplete recovery of strain upon unloading from a loading state in between the two yield points has also been observed in other metastable β -type Ti–Nb-based alloys [41–43]. This means that irrecoverable deformation (e.g., dislocation slip and deformation twinning) is already introduced prior to the second yield point in these alloys.

The evolution of individual α'' martensite plate and $\{332\}$ twin upon loading and unloading is more clearly revealed in Fig. 4e. In addition to the increase in their number density, their thickness increases as well with increasing strain. It is also observed that some $\{332\}$ twins cut through the preformed α'' martensite plates, demonstrating that the α'' martensite plates do not act as effective obstacles against twin propagation. Upon unloading, the partial detwinning of the $\{332\}$ twins is shown to proceed via shrinkage along their transverse direction. This is in sharp contrast to the thermally-activated detwinning process of $\{332\}$ twins, which is characterized by the retreat of the twin tips [16,47].

Fig. 5 shows the TEM analysis of a through-thickness TEM lamella prepared from the location marked by a coarse line section in Fig. 4e, which contains the two types of deformation bands

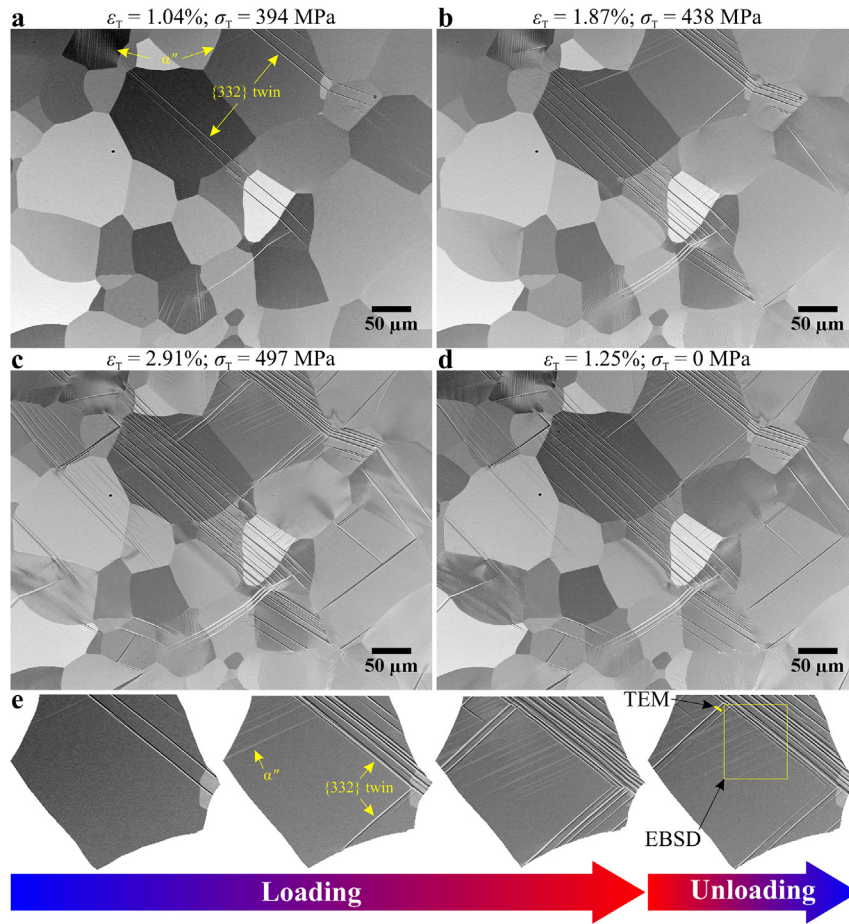


Fig. 4. Evolution of deformation microstructures observed on the pre-polished surface of a water quenched tensile specimen upon loading and unloading (tensile direction: horizontal). (a–c) Sequential BSE images taken from the same region at different strain levels upon loading. (d) BSE image of the same region after unloading. (e) Close-up images of the same grain located on the top right side of (a–d).

mentioned above. A low-magnification overview of this lamella is displayed in Fig. 5a, where the cross section of four deformation bands (labelled as I–IV) can be seen. On the surface, Band I exhibits distinct topographic contrast, while Band III and Band IV show only weak channeling contrast. As illustrated in Fig. 5a, the inclined surface step produced by Band I has a height of roughly 158 nm, while a negligible surface relief is revealed for Band III and Band IV. When viewed along the $[1\bar{1}0]_{\beta}$ zone axis, Fig. 5b, parallel features are shown in Band I and Band III. The SAED patterns (Fig. 5c–f) acquired along this zone axis demonstrate that Band I is a $\{332\}$ twin, while the other three parallel bands (II, III and IV) are α'' martensite plates. The parallel features within Band I, thus, correspond to the characteristic internal sub-microstructures of $\{332\}$ twin – parallel dislocations [16]. The rotation angle between the twin and matrix lattices, determined from Fig. 5c and d, is about 50.5° , implying that the twin/matrix interface is a $\Sigma 11$ boundary within the coincidence site lattice (CSL) theory [48]. Fig. 5d and f also reveal that the orientation relationship between the β matrix and the stress-induced α'' martensite is $[1\bar{1}0]_{\beta} // [00\bar{1}]_{\alpha''}$ and $(112)_{\beta} // (110)_{\alpha''}$, identical to that for thermally induced α'' martensite [49]. Although not unambiguously identified here, we expect that the parallel sub-microstructures in Band III are also dislocations, as observed in the stress-induced martensite plates of other bcc and face-centered cubic (fcc) alloys [50,51]. More detailed analysis is currently being carried out to clarify the sub-microstructures within the stress-induced α'' martensite plates and the results

will be published elsewhere.

Fig. 6 shows the EBSD analysis of the region framed by a rectangle in Fig. 4e. Due to the pseudo-cubic symmetry of the α'' Kikuchi patterns [16], the orthorhombic α'' martensite was also indexed as bcc β phase by the EBSD data collecting software (OIMDC 7.3.1) with an average confidence index value above 90%. However, the $\{332\}$ twins and α'' martensite plates can be distinguished by their different contrast in the image quality (IQ) map, Fig. 6a, and by their different crystallographic orientations in the inverse pole figure (IPF) map, Fig. 6b. It is clearly revealed that the $\{332\}$ twins, as directly evidenced by their $\Sigma 11$ boundaries (Fig. 6a), correspond to the deformation bands with distinct topographic contrast shown in the BSE images (Fig. 4). In the IPF map of Fig. 6b, the color (crystallographic orientation) of the α'' martensite plates is only slightly different from that of the matrix, indicating that the crystal rotation associated with the $\beta \rightarrow \alpha''$ martensitic transformation [52] is relatively small. This is in line with the rather small misorientation angles ($<1.6^\circ$) generated by the martensite plates, as illustrated in Fig. 6c. It should be noted that in some grains of the present WQ material an additional layer with different rotation angle boundaries was also observed adjacent to certain $\{332\}$ twins (Supplementary Fig. S2), resembling that in the coarse-grained ($\sim 1000 \mu\text{m}$) Ti–36Nb–2Ta–3Zr alloy [16].

Similar to the early stage of plastic deformation (Fig. 4), both deformation twinning and stress-induced martensitic transformation are also intensely activated during the constant work

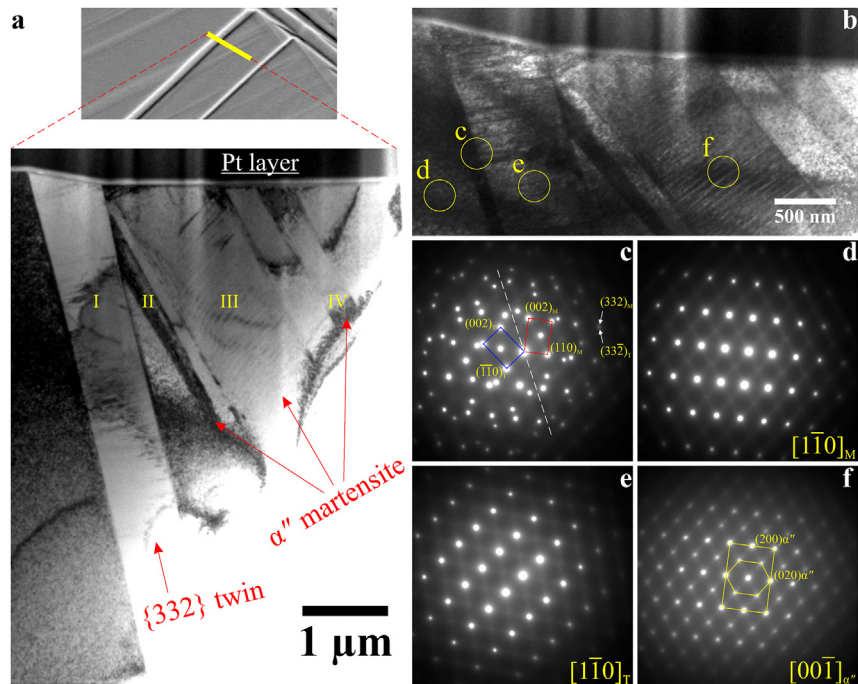


Fig. 5. TEM analysis of the through-thickness TEM lamella prepared from the location marked by a yellow coarse line section in Fig. 4e. (a) Low-magnification overview of the lamella. (b) TEM bright field image of the lamella viewed along the $[1\bar{1}0]_{\beta}$ direction. (c–f) Selected area electron diffraction patterns acquired from the circled regions in (b). The index in the bottom right corner of (d–f) shows the corresponding zone axis, where the subscripts “M” and “T” represent “matrix” and “twin”, respectively. (For interpretation of the references to color in this figure legend, the reader is referred to the Web version of this article.)

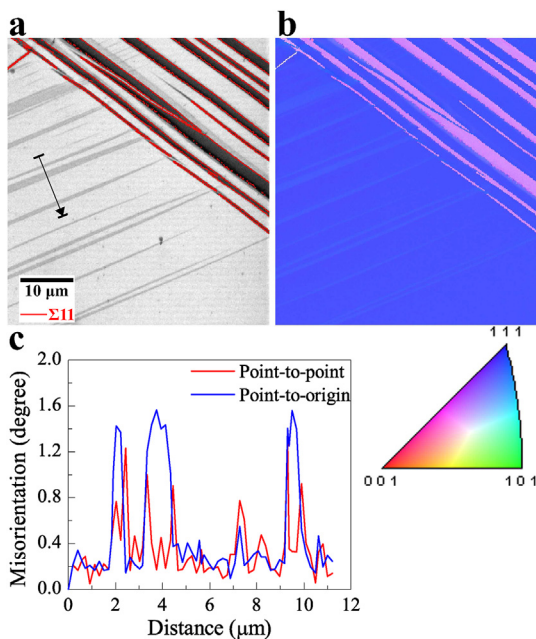


Fig. 6. EBSD analysis of the region framed by a yellow rectangle in Fig. 4e. (a) Image quality map overlaid with $\Sigma 11$ boundaries. (b) Inverse pole figure map and the corresponding legend. (c) Misorientation profiles along the arrow in (a). (For interpretation of the references to color in this figure legend, the reader is referred to the Web version of this article.)

hardening stage (Stage II shown in Fig. 3b) of the WQ material, as illustrated in Fig. 7. The BSE image in Fig. 7a shows that the representative deformation microstructures in this stage are characterized by in-grain misorientations as well as densely spaced

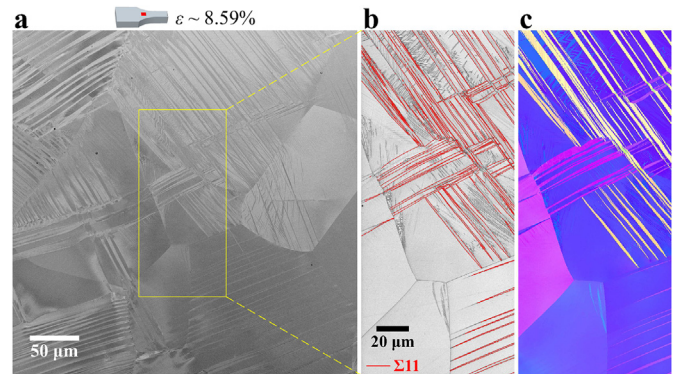


Fig. 7. Deformation microstructures of the Ti–25Nb–0.7Ta–2Zr alloy in water quenched state at a global deformation strain of 8.59%. (a) BSE image taken from a failed tensile specimen (schematically illustrated on top), which was subjected to grinding and polishing after failure. The strain of the imaging area (in red) was determined by digital image correlation measurements. (b) Image quality map overlaid with $\Sigma 11$ boundaries and (c) inverse pole figure map of the framed region in (a). The legend of (c) is the same as that of Fig. 6b. (For interpretation of the references to color in this figure legend, the reader is referred to the Web version of this article.)

long deformation bands subdividing the grains. EBSD analysis (Fig. 7b and c) demonstrates that these long deformation bands are $\{332\}$ twins with $\Sigma 11$ boundaries. In between these twins and even inside some of the individual twins, numerous α'' martensite plates occur, as clearly shown in Fig. 7b and evidenced by their slight orientation difference with respect to the adjacent β structure (Fig. 7c). It is important to note that some of the martensite plates are distorted or segmented by slip traces, which should be attributed to the local dislocation flux that surrounds or cuts through them. Nevertheless, most of the twins are still straight at this strain level, indicating that the $\{332\}$ twins are more effective obstacles

against dislocation motion compared to the α'' martensite plates. In the IPF map of Fig. 7c, we can also see in-grain misorientations (color gradients) in the regions free of twin and martensite (e.g., the regions near the bottom left grain boundary). These misorientations should also result from the local dislocation flux [53].

When the WQ material is deformed to a higher strain of 17.82%, corresponding to Stage III shown in Fig. 3b, the area fraction of the {332} twins reaches about 40% and a large number of slip traces is observed (Fig. 8). In contrast to lower strain levels (Figs. 4 and 7), most of the twins in this regime are highly distorted. This means that in Stage III the nucleation and propagation of deformation twins may have ceased. The microstructural evolution with increasing strain in this stage may thus be governed by dislocation activities. A recent study on the mechanism of TWIP in β -type Ti–15 wt% Mo alloy has also revealed that the deformation twinning activities are saturated at the end of the constant work hardening stage and the subsequent microstructural evolution is dominated by the rapid increase in dislocation density [19].

3.3.2. Dislocation channels in the FC material

Besides the work hardening behavior, the deformation microstructures of the present ω -enriched FC material are also akin to the ω -enriched gum metal [27], characterized by ω -devoid dislocation channels (Fig. 9) throughout the entire plastic deformation process. No deformation twin or stress-induced martensite was observed in the deformed FC material, demonstrating that the plastic deformation is mainly carried by dislocations moving in the dislocation channels [27]. Fig. 9a shows an example of the deformation microstructures in the FC material. It is clearly revealed that the plastic deformation is localized into a series of dislocation channels. Fig. 9b displays the scanning transmission electron microscopy (STEM) bright field image of a TEM lamella, which extends across a dislocation channel (Fig. 9a). In this image, the channel is visualized by dark contrast as well as a pronounced surface step. The dark contrast should result from the profuse tangled dislocations stored within the channel, as revealed in our previous work [27]. The height of the surface step is ~ 250 nm, implying that hundreds of $a_\beta/2\langle 111 \rangle_\beta$ (a_β is the lattice parameter of the bcc β phase [16]) dislocations have moved through the channel and escaped out of the free surface. Two other important features illustrated in Fig. 9b are the varying width (~ 50 – 230 nm) and the non-flat boundaries of the channel, which indicate that polyslip rather than single planar

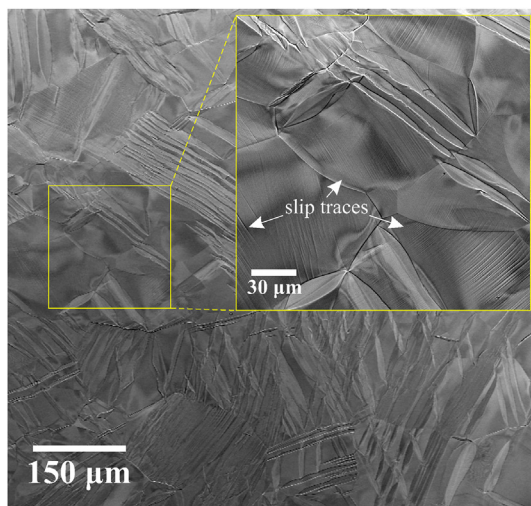


Fig. 8. BSE images taken from the pre-polished surface of a water quenched tensile specimen when strained to 17.82% (tensile direction: horizontal).

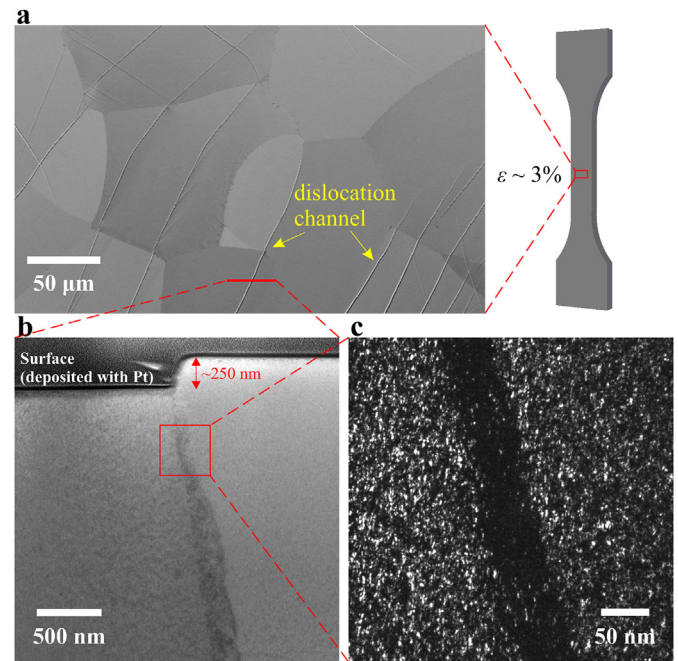


Fig. 9. Representative deformation microstructures of the Ti–25Nb–0.7Ta–2Zr alloy in furnace cooled state. (a) BSE image taken from the pre-polished surface of a tensile specimen after deformation to roughly 3% plastic strain. (b) STEM bright field image of the through-thickness TEM lamella prepared from the location marked by a red coarse line section in (a). (c) TEM dark field image acquired using an ω reflection. (For interpretation of the references to color in this figure legend, the reader is referred to the Web version of this article.)

slip occurred within the channel during straining [54,55], i.e., multiple slip systems were activated within the channel. We have revealed that each of the four ω variants can be removed (via $\omega \rightarrow \beta$ transformation) by the dissociation and slip of the corresponding $\{112\}_\beta \langle 111 \rangle_\beta$ dislocations [27]. The significant depletion of ω particles within the dislocation channel (Fig. 9c) can thus be explained by such dislocation activities.

4. Discussion

The results reveal that the metastable β -type Ti–25Nb–0.7Ta–2Zr alloy, when rendered either ω -free or ω -enriched, exhibits significantly different deformation behavior. For the ω -free WQ material, α'' martensite and {332} twin are formed during plastic deformation, leading to high work hardening. In contrast, the ω -enriched FC material behaves like the ω -enriched gum metal [27], showing localized dislocation plasticity inside specific ω -devoid channels and relatively low work hardening. Below we discuss the deformation mechanisms of these two materials as well as the effect of ω precipitation on the deformation mechanisms.

4.1. Mechanisms of plastic deformation

As revealed in Figs. 4–8, multiple deformation mechanisms, including stress-induced martensitic transformation, deformation twinning and dislocation slip, occur during tensile deformation in the ω -free WQ material. The plastic strain accommodated by the martensitic transformation is, however, negligibly small, as evidenced by the negligible surface relieves produced by the α'' martensite plates (Fig. 5a and b). The maximum plastic strain that can be accommodated by {332} twinning is $s = 35.36\%$ [16,56],

which only occurs when the gauge section of the tensile specimen is a properly-oriented single crystal and is completely twinned along the corresponding $\langle 113 \rangle_\beta$ twinning direction. Assuming an average Taylor factor of $M = 2.754$ for the present polycrystalline WQ material [57], this twinning mode could potentially produce a maximum strain of $s/M = 12.84\%$ when the entire volume of the polycrystalline gauge section is twinned. Thus, the total strain accommodated by $\{332\}$ twinning in the WQ material is actually rather small in comparison to the large elongation to fracture (57%) observed for this material. Most of the plastic deformation in this material is, therefore, carried by dislocation slip. However, the formation of α'' martensite plates and $\{332\}$ twins during plastic deformation leads to continuous grain subdivision by introducing new sharp interfaces. These interfaces act as barriers to dislocation motion and thus reduce the dislocation mean free path, resulting in additional work hardening, a phenomenon referred to as “dynamic Hall–Petch effect” [21]. The fact that the martensite plates are more easily cut through by moving dislocations (Fig. 7) implies that the additional work hardening is primarily contributed by the twins. The enhanced work hardening caused by the introduction of twin and martensite postpones the onset of necking to higher strain levels and hence increase the uniform elongation of the WQ material, i.e., giving rise to the TRIP and TWIP effects [23].

With the presence of large numbers of nanometer-sized ω particles ($3.20 \pm 0.78 \times 10^{24} \text{ m}^{-3}$), the $\beta \rightarrow \alpha''$ martensitic transformation and $\{332\}$ twinning are completely suppressed in the FC material. Our results reveal that the plastic deformation of this material is governed by dislocation channeling, i.e., localized dislocation slip in a series of ω -devoid channels (Fig. 9). The formation mechanism of the ω -devoid dislocation channels has been discussed in detail in our previous work [27], which suggests that the ω particles are cut through by moving dislocations on the $\{112\}_\beta$ slip planes as $\{112\}_\beta$ is parallel to the prismatic slip plane $\{1\bar{1}00\}_\omega$ of the ω phase and this process promotes the $\omega \rightarrow \beta$ transformation, i.e., removing the ω particles. As mentioned above, the present study also reveals that polyslip rather than single planar slip occurs within the ω -devoid channels. We thus expect that multiple slip systems on different $\{112\}_\beta$ slip planes are activated and remove all four ω variants in each of the differently aligned channels.

4.2. Role of ω precipitation in suppressing the TWIP and TRIP effects

Previous studies [15,20,58–60] have suggested that the deformation mechanisms of β titanium alloys are dependent on the β phase stability: the plastic deformation of stable β titanium alloys is dominated by dislocation slip, while additional deformation twinning and stress-induced martensitic transformation can be activated in metastable β titanium alloys. It should be noted that the stability of the β matrix in metastable β titanium alloys could be enhanced when secondary phases are precipitated. For instance, the precipitation of ω or α' phase involves the diffusion of β -stabilizing elements (V, Mo, Nb, Ta, etc.) out of the precipitates and into the adjacent β matrix, resulting in the enrichment of β -stabilizing elements in the β matrix [61,62]. Such elemental partitioning enhances the stability of the β matrix and is thus expected to suppress the activation of deformation twinning and martensitic transformation. Recently, Mantri et al. [62] have observed that the precipitation of ω phase in Ti–12 wt% Mo alloy after annealing at 475 °C for 48 h gives rise to a significantly stabilized β matrix (with 27 wt% Mo) and changes the deformation mode from twinning to slip. Thus, we first expected that the suppression of TWIP and TRIP effects in the present ω -enriched FC material may be due to the enhanced β phase stability resulting from the elemental partitioning between the β and ω phases. In order to clarify this point, we conducted APT experiments to analyze the average

compositions of the β matrix and ω precipitate in both the WQ and the FC materials.

The 3D APT reconstruction of the WQ and FC materials prior to deformation is shown in the upper and lower panels of Fig. 10a, respectively. For the WQ material, the corresponding APT reconstruction exhibits a random distribution of alloying elements. The average composition of the WQ material measured by APT is listed in Table 2. In contrast, elemental partitioning, characterized by the rejection of Nb from a number of nanometer-sized domains, is observed in the APT reconstruction of the FC material. These Nb-lean domains, corresponding to the ω particles [61,62], are highlighted by 76 at.% Ti iso-concentration surfaces in Fig. 10a. To quantitatively illustrate the elemental partitioning between the β and ω phases, an analysis cylinder passing through several ω particles was placed in the APT reconstruction of the FC material (lower panel of Fig. 10a). The 1D concentration profile along this cylinder (Fig. 10b) clearly reveals the rejection of Nb from the ω particles. We further quantified the average concentration profiles across the β/ω interface using proximity histogram (proxigram) [63], as shown in Fig. 10c. The average compositions of the β matrix and ω precipitate in the FC material, obtained from the proxigram, are summarized in Table 2. We can see that in addition to Nb, Ta and Zr are also rejected from the ω precipitate. The average concentration of the Nb, Ta and Zr inside the ω precipitate is reduced by 60%, 45% and 22%, respectively, compared to that in the β matrix. This means that all of these three solutes act as ω -destabilizers (similar to V, Mo, Cr and Al [61,62]), which diffuse into the β matrix during ω precipitation. In fact, it has been revealed in Ti–12 wt% Mo alloy that the ω precipitates seem to have the tendency to turn into nearly pure-Ti domains with their continuous growth and the associated partitioning effects outlined above [62]. We find that the elemental partitioning associated with the ω precipitation observed in the FC material actually brings about very little enrichment of β -stabilizing elements (Nb and Ta) in the β matrix. The increase in the average concentration of Nb and Ta is 0.77 at.% and 0.02 at.%, respectively. This should be attributed to the rather small volume fraction ($0.31 \pm 0.08\%$) of the ω phase in the FC material. Although the critical concentrations of the β -stabilizing elements for suppressing the stress-induced $\beta \rightarrow \alpha''$ martensitic transformation and $\{332\}$ twinning are not well known, here we conclude that the suppression of these two deformation mechanisms in the FC material is not due to the slightly enhanced stability of the β matrix (Ti–26.38Nb–0.44Ta–2.14Zr, at.%), since these two deformation mechanisms have been observed in an even more stable Ti–27 at.% Nb alloy [64].

After ruling out the possibility of enhanced β phase stability in suppressing the TWIP and TRIP effects, we now consider the resistance of the ω phase to these two effects. At the atomic scale, the $\beta \rightarrow \alpha''$ martensitic transformation is primarily mediated by the shuffling of $\{1\bar{1}0\}_\beta$ planes along $\langle 110 \rangle_\beta$ directions [65]. The shear modulus along the $\{1\bar{1}0\}_\beta \langle 110 \rangle_\beta$ direction is C' , which assumes a very small value ($< 18 \text{ GPa}$) for the β compositions studied here [7,9,66], corresponding to a strong propensity for martensitic transformation. According to the orientation relationship between β and ω (Fig. 2), the $\{1\bar{1}0\}_\beta$ plane is parallel to the secondary prismatic plane $\{11\bar{2}0\}_\omega$ of the ω phase. The shear modulus on the $\{11\bar{2}0\}_\omega$ plane can be calculated by $G_{\text{spm}} = 2/(S_{44} + 2S_{11} - 2S_{12})$, where S_{ij} is the elastic compliance of the ω phase [67]. Due to the difficulty in preparing a bulk material consisting of a single ω phase, the elastic constants C_{ij} (inverse of S_{ij}) of the ω phase have rarely been experimentally measured. To the best of our knowledge, experimental data for the C_{ij} of the ω phase are only available for pure titanium [68]. For Ti–Nb system, theoretical data for the C_{ij} of the ω phase are available for a composition of Ti–25 at.% Nb [69]. Recent ab initio calculations suggest an approximately linear

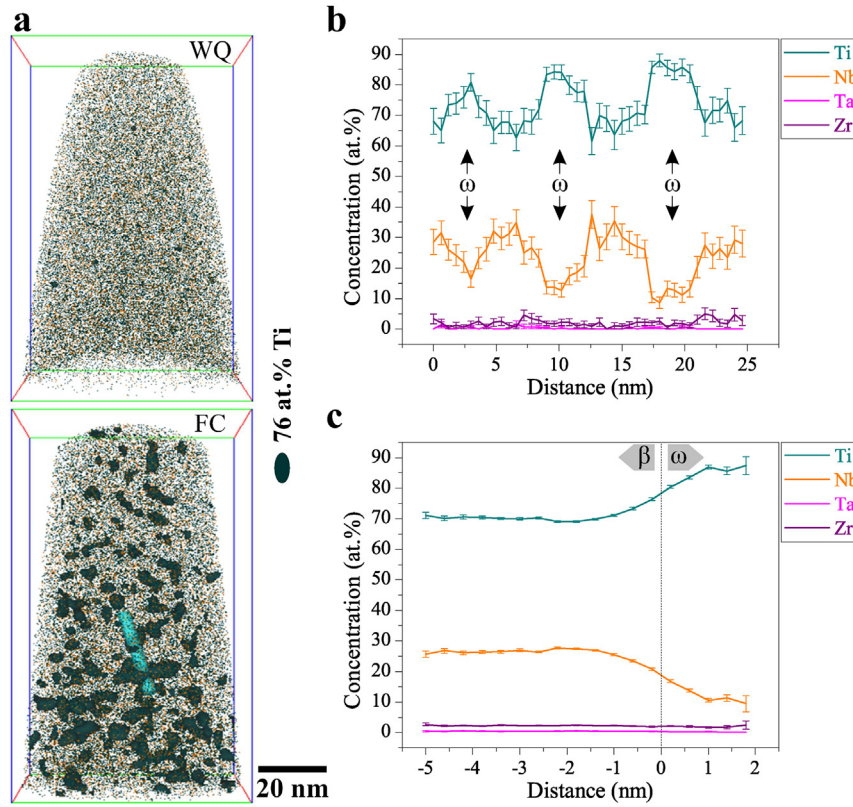


Fig. 10. APT analysis of the Ti–25Nb–0.7Ta–2Zr alloy in water quenched (WQ) and furnace cooled (FC) states prior to deformation. (a) 3D reconstruction of two APT specimens with 76 at.% Ti iso-concentration surfaces showing the ω particles. The upper WQ specimen is revealed to be ω -free, while many ω particles are shown in the lower FC specimen. (b) 1D concentration profile along the cyan cylinder (3.5 nm diameter) indicated in (a). (c) Proxigram of the ω particles in the FC specimen showing the average concentration of various elements as a function of the distance from the β/ω interface. (For interpretation of the references to color in this figure legend, the reader is referred to the Web version of this article.)

Table 2

Chemical compositions (in at.%) of the β matrix and ω precipitate measured by APT in the Ti–25Nb–0.7Ta–2Zr alloy. WQ and FC represent the ω -free water quenched and the ω -enriched furnace cooled states of this alloy, respectively.

Element	WQ	FC	
	β	β	ω
Ti	71.44 ± 0.06	70.44 ± 0.51	86.98 ± 0.67
Nb	25.61 ± 0.04	26.38 ± 0.49	10.52 ± 0.61
Ta	0.42 ± 0.01	0.44 ± 0.07	0.24 ± 0.10
Zr	2.04 ± 0.01	2.14 ± 0.16	1.67 ± 0.26

relationship between C_{ij} and solute concentration for the ω phase of Ti–Mo system [70]. Here, we assume that such a linear relationship also applies for the current Ti–Nb-based system. Thus, the C_{ij} of the present ω phase (approximated by Ti–11 at.% Nb, Table 2) can be estimated by linear interpolation between the experimental data for pure titanium and the theoretical data for Ti–25 at.% Nb. With the obtained C_{ij} values, G_{spm} is calculated to be 39.55 GPa, which is much larger than C . This implies that the ω phase is a strong obstacle to the collective $\{1\bar{1}0\}_{\beta} <110>_{\beta}$ atomic movements involved in the martensitic transformation. Thus, the densely distributed ($l_0 = 11.53 \pm 1.37$ nm) ω particles in the FC material act as local barriers to prevent long-range martensitic transformation, i.e., suppressing the TRIP effect. A similar phenomenon has been observed in oxygen-added β -Ti alloys, where long-range martensitic transformation is suppressed by randomly distributed nanometer-sized lattice modulation domains [71].

Recently, the mechanism of $\{332\}$ twinning in metastable β

titanium alloys was extensively studied [16,56,64]. The available experimental results point to a strong correlation between long-range α'' martensite and $\{332\}$ twin. Although the detailed formation pathway is still under debate, $\{332\}$ twin is regarded to be formed from α'' martensite [16,64]. Therefore, when the long-range martensitic transformation is prevented by ω particles, the TWIP effect will also be suppressed.

4.3. Effect of ω phase on dislocation plasticity

As mentioned above, the solute-depleted ω particles in the FC material are supposed to be cut through by moving dislocations on the $\{112\}_{\beta}/\{\bar{1}100\}_{\omega}$ planes. The resistance of the ω particles to moving dislocations, i.e., the ω -induced increase in the critical resolved shear stress $\Delta\tau_{\omega}$ for dislocation motion, can thus be estimated by taking into account the modulus hardening ($\Delta\tau_{mod}$), interface hardening ($\Delta\tau_{int}$) as well as coherency hardening ($\Delta\tau_{coh}$) effects of the ω particles [72]. However, due to their extremely fine size (~ 1.23 nm), very small volume fraction ($0.31 \pm 0.08\%$) and very low coherency strain [13,73], the latter two effects ($\Delta\tau_{int}$ and $\Delta\tau_{coh}$) are negligible. The yield stress of the FC material can thus be expressed as

$$\sigma_{y, FC} = \sigma_c + M(\Delta\tau_{mod} + \Delta\tau_{int} + \Delta\tau_{coh}) \approx \sigma_c + M\Delta\tau_{mod}, \quad (1)$$

where σ_c is the critical stress required to sustain dislocation motion in the ω -free material. $\Delta\tau_{mod}$ arises from the difference in shear modulus between β and ω , $|G_{\beta} - G_{\omega}|$. According to the equation proposed by Melander and Persson [74], it is given by

$$\Delta\tau_{\text{mod}} = 0.9\sqrt{r_0f_0} \frac{T}{b} \left(\frac{|G_\beta - G_\omega|}{G_\beta} \frac{1}{2b \ln(l_0/b)} \right)^{3/2}, \quad (2)$$

where $r_0 = d_0/2$ is the average radius the ω particles and b is the magnitude of the Burgers vector of the $a_\beta/2\langle 111 \rangle_\beta$ dislocation. T is the dislocation line tension, which is approximated by $G_\beta b^2/2$. Here, the calculated result for $\Delta\tau_{\text{mod}}$ is 44 MPa. Thus, σ_c is roughly 360 MPa, which is slightly higher than the first yield point observed for the ω -free WQ material (Fig. 3a). This supports the claim that the first yield point in the Ti–Nb-based alloys with a double-yielding phenomenon corresponds to the onset of martensitic transformation rather than dislocation slip [39–43].

In the ω -enriched FC material, the above estimated value of $\Delta\tau_\omega$ is the minimum resistance of the ω particles to dislocation motion. Under the circumstances that the slip plane of the moving dislocations is nonparallel to any slip plane of the ω particles, the dislocations will need to bypass the particles, which requires a much higher stress ($\Delta\tau_\omega \sim 214$ MPa) according to the Orowan equation [72]. Thus, the ω particles in between the ω -devoid channels are effective obstacles to dislocation motion. Due to the substantial depletion of ω particles, these channels become easier paths for further dislocation motion, leading to localized dislocation plasticity.

5. Conclusions

Two different starting states of a metastable β -type Ti–25Nb–0.7Ta–2Zr alloy were generated by either water quenching or furnace cooling the alloy sheets after solution treatment in the β phase region. The mechanical response of this alloy in these two states was investigated by tensile tests. The microstructures before and after tensile deformation were examined by SEM, EBSD, TEM and APT. Based on the experimental observations, we draw the following conclusions:

- The two different cooling methods after solution treatment (1000 °C, 1h), water quenching and furnace cooling, have little effect on the grain size and texture. However, the water quenched alloy is ω -free, while the furnace cooled alloy contains a high number density ($3.20 \pm 0.78 \times 10^{24} \text{ m}^{-3}$) of nanometer-sized (~ 1.23 nm) ω particles.
- The ω -free alloy shows a double-yielding phenomenon. Its plastic deformation is mediated by multiple deformation mechanisms, including stress-induced $\beta \rightarrow \alpha''$ martensitic transformation, {332} twinning and dislocation slip. The former two induce joint TRIP and TWIP effects, leading to pronounced work hardening behavior, while the latter one carries the majority of the plastic strain. The {332} twins are more effective obstacles against dislocation motion compared to the stress-induced α'' martensite plates. The plastic strain accommodated by the martensite plates is negligible. During straining, these plates can be cut through by moving dislocations and propagating twins. The nucleation and propagation of {332} twins start prior to the second yield point and cease before the onset of necking. Upon unloading before the second yield point, these twins are subjected to partial detwinning.
- In the ω -enriched alloy, the presence of densely distributed (11.53 ± 1.37 nm inter-particle spacing) ω particles fully suppresses the stress-induced martensitic transformation and {332} twinning. This alloy plastically deforms via dislocation channeling, exhibiting relatively low work hardening. Its deformation microstructures are characterized by ω -devoid dislocation channels. These channels have varying widths and

non-flat boundaries, corresponding to polyslip rather than single planar slip during straining.

- The ω particles show substantial depletion of all solutes (Nb, Ta and Zr). However, due to their low volume fraction ($0.31 \pm 0.08\%$), the enrichment of solutes in the β matrix cannot sufficiently stabilize the β matrix to impede martensitic transformation and {332} twinning. It is the shear modulus difference between β and ω that renders the ω particles act as local barriers to martensitic transformation and {332} twinning, thus suppressing the TRIP and TWIP effects.

Appendix A. Supplementary data

Supplementary data related to this article can be found at <https://doi.org/10.1016/j.actamat.2018.03.053>.

References

- [1] D. Banerjee, J.C. Williams, Perspectives on titanium science and technology, *Acta Mater.* 61 (2013) 844–879.
- [2] J.C. Williams, B.S. Hickman, H.L. Marcus, The effect of omega phase on the mechanical properties of titanium alloys, *Metall. Trans.* 2 (1971) 1913–1919.
- [3] A. Devaraj, V.V. Joshi, A. Srivastava, S. Manandhar, V. Moxson, V.A. Duz, C. Lavender, A low-cost hierarchical nanostructured beta-titanium alloy with high strength, *Nat. Commun.* 7 (2016), 11176.
- [4] J.D. Cotton, R.D. Briggs, R.R. Boyer, S. Tamirisakandala, P. Russo, N. Shchetnikov, J.C. Fanning, State of the art in beta titanium alloys for airframe applications, *JOM* 67 (2015) 1281–1303.
- [5] O.M. Ivasishin, P.E. Markovsky, Y.V. Matviychuk, S.L. Semiatin, C.H. Ward, S. Fox, A comparative study of the mechanical properties of high-strength β -titanium alloys, *J. Alloy. Comp.* 457 (2008) 296–309.
- [6] T. Saito, T. Furuta, J.H. Hwang, S. Kuramoto, K. Nishino, N. Suzuki, R. Chen, A. Yamada, K. Ito, Y. Seno, T. Nonaka, H. Ikehata, N. Nagasako, C. Iwamoto, Y. Ikuhara, T. Sakuma, Multifunctional alloys obtained via a dislocation-free plastic deformation mechanism, *Science* 300 (2003) 464–467.
- [7] R.J. Talling, R.J. Dashwood, M. Jackson, S. Kuramoto, D. Dye, Determination of ($C_{11}-C_{12}$) in Ti–36Nb–2Ta–3Zr–0.30 (wt.%) (Gum metal), *Scripta Mater.* 59 (2008) 669–672.
- [8] H. Xing, J. Sun, Mechanical twinning and omega transition by $\langle 111 \rangle$ {112} shear in a metastable β titanium alloy, *Appl. Phys. Lett.* 93 (2008), 031908.
- [9] R.J. Talling, R.J. Dashwood, M. Jackson, D. Dye, On the mechanism of super-elasticity in Gum metal, *Acta Mater.* 57 (2009) 1188–1198.
- [10] M. Besse, P. Castany, T. Gloriant, Mechanisms of deformation in gum metal TNTZ-O and TNTZ titanium alloys: a comparative study on the oxygen influence, *Acta Mater.* 59 (2011) 5982–5988.
- [11] E. Plancher, C.C. Tasan, S. Sandloebes, D. Raabe, On dislocation involvement in Ti–Nb gum metal plasticity, *Scripta Mater.* 68 (2013) 805–808.
- [12] Y. Yang, S.Q. Wu, G.P. Li, Y.L. Li, Y.F. Lu, K. Yang, P. Ge, Evolution of deformation mechanisms of Ti–22.4Nb–0.73Ta–2Zr–1.34O alloy during straining, *Acta Mater.* 58 (2010) 2778–2787.
- [13] M.J. Lai, C.C. Tasan, J. Zhang, B. Grabowski, L.F. Huang, D. Raabe, Origin of shear induced β to ω transition in Ti–Nb-based alloys, *Acta Mater.* 92 (2015) 55–63.
- [14] M. Marteleur, F. Sun, T. Gloriant, P. Vermaut, P.J. Jacques, F. Prima, On the design of new β -metastable titanium alloys with improved work hardening rate thanks to simultaneous TRIP and TWIP effects, *Scripta Mater.* 66 (2012) 749–752.
- [15] F. Sun, J.Y. Zhang, M. Marteleur, T. Gloriant, P. Vermaut, D. Laillé, P. Castany, C. Curfs, P.J. Jacques, F. Prima, Investigation of early stage deformation mechanisms in a metastable β titanium alloy showing combined twinning-induced plasticity and transformation-induced plasticity effects, *Acta Mater.* 61 (2013) 6406–6417.
- [16] M.J. Lai, C.C. Tasan, D. Raabe, On the mechanism of {332} twinning in metastable β titanium alloys, *Acta Mater.* 111 (2016) 173–186.
- [17] O. Bouaziz, S. Allain, C.P. Scott, P. Cugy, D. Barbier, High manganese austenitic twinning induced plasticity steels: a review of the microstructure properties relationships, *Curr. Opin. Solid State Mater. Sci.* 15 (2011) 141–168.
- [18] D.R. Steinmetz, T. Jäpel, B. Wietbrock, P. Eisenlohr, I. Gutierrez-Urrutia, A. Saeed-Akbari, T. Hickel, F. Roters, D. Raabe, Revealing the strain-hardening behavior of twinning-induced plasticity steels: theory, simulations, experiments, *Acta Mater.* 61 (2013) 494–510.
- [19] X. Min, X. Chen, S. Emura, K. Tsuchiya, Mechanism of twinning-induced plasticity in β -type Ti–15Mo alloy, *Scripta Mater.* 69 (2013) 393–396.
- [20] F. Sun, J.Y. Zhang, M. Marteleur, C. Brozek, E.F. Rauch, M. Veron, P. Vermaut, P.J. Jacques, F. Prima, A new titanium alloy with a combination of high strength, high strain hardening and improved ductility, *Scripta Mater.* 94 (2015) 17–20.
- [21] I. Gutierrez-Urrutia, D. Raabe, Dislocation and twin substructure evolution during strain hardening of an Fe–22 wt.% Mn–0.6 wt.% C TWIP steel observed by electron channeling contrast imaging, *Acta Mater.* 59 (2011) 6449–6462.

- [22] I. Gutierrez-Urrutia, D. Raabe, Multistage strain hardening through dislocation substructure and twinning in a high strength and ductile weight-reduced Fe–Mn–Al–C steel, *Acta Mater.* 60 (2012) 5791–5802.
- [23] S.L. Wong, M. Madivala, U. Prahll, F. Roters, D. Raabe, A crystal plasticity model for twinning- and transformation-induced plasticity, *Acta Mater.* 118 (2016) 140–151.
- [24] J. Wang, Z. Zeng, C.R. Weinberger, Z. Zhang, T. Zhu, S.X. Mao, In situ atomic-scale observation of twinning-dominated deformation in nanoscale body-centred cubic tungsten, *Nat. Mater.* 14 (2015) 594–600.
- [25] M. Ahmed, D. Wexler, G. Casillas, O.M. Ivasishin, E.V. Pereloma, The influence of β phase stability on deformation mode and compressive mechanical properties of Ti–10V–3Fe–3Al alloy, *Acta Mater.* 84 (2015) 124–135.
- [26] M. Ahmed, D. Wexler, G. Casillas, D.G. Savvakis, E.V. Pereloma, Strain rate dependence of deformation-induced transformation and twinning in a metastable titanium alloy, *Acta Mater.* 104 (2016) 190–200.
- [27] M.J. Lai, C.C. Tasan, D. Raabe, Deformation mechanism of ω -enriched Ti–Nb-based gum metal: dislocation channeling and deformation induced ω – β transformation, *Acta Mater.* 100 (2015) 290–300.
- [28] C.C. Tasan, M. Diehl, D. Yan, C. Zambaldi, P. Shanthraj, F. Roters, D. Raabe, Integrated experimental–simulation analysis of stress and strain partitioning in multiphase alloys, *Acta Mater.* 81 (2014) 386–400.
- [29] T. Malis, S.C. Cheng, R.F. Egerton, EELS log-ratio technique for specimen-thickness measurement in the TEM, *J. Electron. Microsc. Tech.* 8 (1988) 193–200.
- [30] T. Yano, Y. Murakami, D. Shindo, Y. Hayasaka, S. Kuramoto, Transmission electron microscopy studies on nanometer-sized ω phase produced in Gum Metal, *Scripta Mater.* 63 (2010) 536–539.
- [31] D. Raabe, K. Lücke, Rolling and annealing textures of bcc metals, *Mater. Sci. Forum* 157–162 (1994) 597–610.
- [32] B. Sander, D. Raabe, Texture inhomogeneity in a Ti–Nb-based β -titanium alloy after warm rolling and recrystallization, *Mater. Sci. Eng. A* 479 (2008) 236–247.
- [33] J.L. Zhang, C.C. Tasan, M.J. Lai, D. Yan, D. Raabe, Partial recrystallization of gum metal to achieve enhanced strength and ductility, *Acta Mater.* 135 (2017) 400–410.
- [34] Y. Hanlumuang, R.P. Sankaran, M.P. Sherburne, J.W. Morris, D.C. Chrzan, Phonons and phase stability in Ti–V approximants to gum metal, *Phys. Rev. B* 85 (2012), 144108.
- [35] E. Sukeidai, H. Hashimoto, M. Tomita, Investigation of omega-phase in Ti–Mo alloys by high resolution electron microscopy, image processing and dark-field methods, *Philos. Mag. A* 64 (1991) 1201–1208.
- [36] S.K. Sikka, Y.K. Vohra, R. Chidambaram, Omega phase in materials, *Prog. Mater. Sci.* 27 (1982) 245–310.
- [37] E. Sukeidai, H. Hashimoto, M. Hida, H. Mabuchi, Formation of ω phase in Ti–Mo alloys after aging and deforming, *Mater. Sci. Technol.* 8 (1992) 3–9.
- [38] G. Gottstein, *Physical Foundations of Materials Science*, Springer-Verlag Berlin Heidelberg, 2004.
- [39] H.Y. Kim, H. Satoru, J.I. Kim, H. Hosoda, S. Miyazaki, Mechanical properties and shape memory behavior of Ti–Nb alloys, *Mater. Trans.* 45 (2004) 2443–2448.
- [40] J.I. Kim, H.Y. Kim, H. Hosoda, S. Miyazaki, Shape memory behavior of Ti–22Nb–(0.5–2.0)O(at%) biomedical alloys, *Mater. Trans.* 46 (2005) 852–857.
- [41] H.Y. Kim, Y. Ikehara, J.I. Kim, H. Hosoda, S. Miyazaki, Martensitic transformation, shape memory effect and superelasticity of Ti–Nb binary alloys, *Acta Mater.* 54 (2006) 2419–2429.
- [42] Y.L. Hao, S.J. Li, S.Y. Sun, C.Y. Zheng, R. Yang, Elastic deformation behaviour of Ti–24Nb–4Zr–7.9Sn for biomedical applications, *Acta Biomater.* 3 (2007) 277–286.
- [43] A. Amarolahy, P. Castany, F. Prima, P. Laheurte, I. Péron, T. Gloriant, Micro-structure and mechanical behavior of superelastic Ti–24Nb–0.5O and Ti–24Nb–0.5N biomedical alloys, *J. Mech. Behav. Biomed.* 9 (2012) 83–90.
- [44] T. Li, J. Zheng, Z. Chen, Description of Full-range Strain Hardening Behavior of Steels, vol. 5, SpringerPlus, 2016, p. 1316.
- [45] U.F. Kocks, H. Mecking, Physics and phenomenology of strain hardening: the FCC case, *Prog. Mater. Sci.* 48 (2003) 171–273.
- [46] S. Zaefferer, N.-N. Elhami, Theory and application of electron channelling contrast imaging under controlled diffraction conditions, *Acta Mater.* 75 (2014) 20–50.
- [47] L. Qu, Y. Yang, Y.F. Lu, L. Feng, J.H. Ju, P. Ge, W. Zhou, D. Han, D.H. Ping, A detwinning process of {332}<113> twins in beta titanium alloys, *Scripta Mater.* 69 (2013) 389–392.
- [48] S. Ranganathan, On the geometry of coincidence-site lattices, *Acta Crystallogr.* 21 (1966) 197–199.
- [49] Y.W. Chai, H.Y. Kim, H. Hosoda, S. Miyazaki, Interfacial defects in Ti–Nb shape memory alloys, *Acta Mater.* 56 (2008) 3088–3097.
- [50] S. Kajiwar, T. Kikuchi, Dislocation structures produced by reverse martensitic transformation in a Cu–Zn alloy, *Acta Metall.* 30 (1982) 589–598.
- [51] S. Kajiwar, Characteristic features of shape memory effect and related transformation behavior in Fe-based alloys, *Mater. Sci. Eng. A* 273–275 (1999) 67–88.
- [52] D.S. Lieberman, M.S. Wechsler, T.A. Read, Cubic to orthorhombic diffusionless phase change: experimental and theoretical studies of AuCd, *J. Appl. Phys.* 26 (1954) 473–484.
- [53] B. Gludovatz, A. Hohenwarther, D. Catoor, E.H. Chang, E.P. George, R.O. Ritchie, A fracture-resistant high-entropy alloy for cryogenic applications, *Science* 345 (2014) 1153–1158.
- [54] U.F. Kocks, Polyslip in single crystals, *Acta Metall.* 8 (1960) 345–352.
- [55] B. Bay, N. Hansen, D.A. Hughes, D. Kuhlmann-Wilsdorf, Overview no. 96 evolution of f.c.c. deformation structures in polyslip, *Acta Metall. Mater.* 40 (1992) 205–219.
- [56] H. Tobe, H.Y. Kim, T. Inamura, H. Hosoda, S. Miyazaki, Origin of {332} twinning in metastable β -Ti alloys, *Acta Mater.* 64 (2014) 345–355.
- [57] J.M. Rosenberg, H.R. Piehler, Calculation of the Taylor factor and lattice rotations for bcc metals deforming by pencil glide, *Metall. Trans.* 2 (1971) 257–259.
- [58] S. Hanada, M. Ozeki, O. Izumi, Deformation characteristics in β phase Ti–Nb alloys, *Metall. Trans. A* 16 (1985) 789–795.
- [59] S. Hanada, T. Yoshio, O. Izumi, Effect of plastic deformation modes on tensile properties of beta titanium alloys, *Trans. Jpn. Inst. Metals* 27 (1986) 496–503.
- [60] S. Hanada, O. Izumi, Correlation of tensile properties, deformation modes, and phase stability in commercial β -phase titanium alloys, *Metall. Trans. A* 18 (1987) 265–271.
- [61] T. Li, D. Kent, G. Sha, L.T. Stephenson, A.V. Ceguerra, S.P. Ringer, M.S. Dargusch, J.M. Cairney, New insights into the phase transformations to isothermal ω and ω -assisted α in near β -Ti alloys, *Acta Mater.* 106 (2016) 353–366.
- [62] S.A. Mantri, D. Choudhuri, T. Alam, V. Ageh, F. Sun, F. Prima, R. Banerjee, Change in the deformation mode resulting from beta-omega compositional partitioning in a Ti–Mo alloy: room versus elevated temperature, *Scripta Mater.* 130 (2017) 69–73.
- [63] O.C. Hellman, J.A. Vandenbroucke, J. Rüsing, D. Isheim, D.N. Seidman, Analysis of three-dimensional atom-probe data by the proximity histogram, *Microsc. Microanal.* 6 (2000) 437–444.
- [64] P. Castany, Y. Yang, E. Bertrand, T. Gloriant, Reversion of a parent {130}<310> α' martensitic twinning system at the origin of {332}<113> β twins observed in metastable β titanium alloys, *Phys. Rev. Lett.* 117 (2016), 245501.
- [65] H.Y. Kim, L. Wei, S. Kobayashi, M. Tahara, S. Miyazaki, Nanodomain structure and its effect on abnormal thermal expansion behavior of a Ti–23Nb–2Zr–0.7Ta–1.2O alloy, *Acta Mater.* 61 (2013) 4874–4886.
- [66] M. Tane, T. Nakano, S. Kuramoto, M. Hara, M. Niinomi, N. Takesue, T. Yano, H. Nakajima, Low Young's modulus in Ti–Nb–Ta–Zr–O alloys: cold working and oxygen effects, *Acta Mater.* 59 (2011) 6975–6988.
- [67] T.C.T. Ting, On anisotropic elastic materials for which Young's modulus $E(n)$ is independent of n or the shear modulus $G(n,m)$ is independent of n and m , *J. Elasticity* 81 (2005) 271–292.
- [68] M. Tane, Y. Okuda, Y. Todaka, H. Ogi, A. Nagakubo, Elastic properties of single-crystalline ω phase in titanium, *Acta Mater.* 61 (2013) 7543–7554.
- [69] J. Sun, Q. Yao, H. Xing, W. Guo, Elastic properties of β , α' and ω metastable phases in Ti–Nb alloy from first-principles, *J. Phys. Condens. Matter* 19 (2007), 486215.
- [70] P. Cao, F. Tian, Y. Wang, Effect of Mo on the phase stability and elastic mechanical properties of Ti–Mo random alloys from ab initio calculations, *J. Phys. Condens. Matter* 29 (2017), 435703.
- [71] M. Tahara, H.Y. Kim, T. Inamura, H. Hosoda, S. Miyazaki, Lattice modulation and superelasticity in oxygen-added β -Ti alloys, *Acta Mater.* 59 (2011) 6208–6218.
- [72] D.J. Lloyd, Precipitation hardening, in: H.J. McQueen, J.P. Bailon, J.I. Dickson, J.J. Jonas, M.G. Akben (Eds.), *The 7th International Conference on the Strength of Metals and Alloys* vol. 3, Pergamon Press, Montreal, Canada, 1985, p. 1745.
- [73] J. Zhang, C.C. Tasan, M.J. Lai, A.C. Dippel, D. Raabe, Complexion-mediated martensitic phase transformation in Titanium, *Nat. Commun. Now.* 8 (2017), 14210.
- [74] A. Melander, P.Å. Persson, The strength of a precipitation hardened AlZnMg alloy, *Acta Metall.* 26 (1978) 267–278.